Phase separation, microstructure and superconductivity in the $Y_{1-x}Pr_xBa_2Cu_3O_y$ compounds



2008 J. Phys.: Condens. Matter 20 395224

(http://iopscience.iop.org/0953-8984/20/39/395224)

J. Phys.: Condens. Matter **20** (2008) 395224 (15pp) doi:10.1088/0953-8984/20/39/395224

# Phase separation, microstructure and superconductivity in the $Y_{1-x}Pr_xBa_2Cu_3O_y$ compounds

**M Calamiotou[1], A Gantis[1], I Margiolaki[2], D Palles[3], E Siranidi[3] and E Liarokapis[3]**

[1] Solid State Physics Department, School of Physics, University of Athens, GR-15784 Athens, Greece
[2] ESRF, BP 220, F-38043 Grenoble Cedex 9, France
[3] Department of Physics, National Technical University of Athens, GR-15780 Athens, Greece

E-mail: mcalam@phys.uoa.gr

Received 4 July 2008, in final form 19 August 2008
Published 4 September 2008
Online at stacks.iop.org/JPhysCM/20/395224

**Abstract**

High resolution synchrotron x-ray powder diffraction combined with micro-Raman spectroscopy are used to investigate the effect of Pr substitution for Y in optimally doped or overdoped polycrystalline $YBa_2Cu_3O_y$ (Y123) compounds. The spectral analysis of the Raman-active $B_{1g}$-symmetry mode indicates a phase separation into coexisting nanoscopic environments consisting of pure Y123 and Pr123 and a mixed (Y–Pr)123 phase of almost the nominal amount of Pr. The Y123 phase disappears at $x \approx 0.6$ where superconductivity is suppressed, while the formation of the pure Pr123 phase is correlated with the increase of local lattice distortions at the Cu and Ba sites, the presence of crystal defects and the increase of microstrains, as obtained by analyzing the anisotropic XRD peak broadening. The comparison of the Ba $A_g$-symmetry phonon shift for the $Y_{1-x}Pr_xBa_2Cu_3O_y$ and $YBa_{2-z}Pr_zCu_3O_y$ compounds as well as lattice dynamic calculations proves that, when Pr substitutes for Y, it also occupies an amount of Ba sites. The data from Pr, La or Ca substitution for Y indicate that loss of superconductivity is correlated with the substitution of Pr, La for Ba and Ca for Y, though the underlying effects may not be the hole filling by these occupancies.

(Some figures in this article are in colour only in the electronic version)

## 1. Introduction

Soon after the discovery of the Y123 compounds it was found that Pr123 is not superconducting, but the underlying mechanism responsible for the suppression of superconductivity is still unknown [1]. In the $R_{1-x}Pr_xBa_2Cu_3O_y$ [(R–Pr)123] compounds (where R = rare earth and Y) the superconducting critical temperature, $T_c$, decreases monotonically with increasing amount of Pr, reaching $T_c \approx 0$ for a critical concentration $x_c$. The value of the critical concentration $x_c$ for the disappearance of superconductivity in the (R–Pr)123 compounds has been found to depend on the difference in the ionic radii of Pr and the other rare earth, implying that size effects play a certain role. For the $Y_{1-x}Pr_xBa_2Cu_3O_y$ [(Y–Pr)123] compound it has been found that $x_c = 0.6$ [1]. Several mechanisms have been proposed for the destruction of superconductivity such as hole filling, pair breaking and hole localization due to the Pr(4f)–O($2p_\pi$) hybridization [1]. The presence of antisite defects, both Pr-on-Ba-site ($Pr_{Ba}$) [2] and Ba-on-Pr-site ($Ba_{Pr}$) [3] has also been considered but the extent of their effect remains controversial.

The structural and electronic inhomogeneities, which seem to constitute intrinsic properties of cuprate superconductors, have not been studied systematically so far and have not been taken into account when interpreting the superconducting properties of (R–Pr)123; nevertheless, the presence of nanometric inhomogeneities, induced by Pr doping, has been proposed to account for the observed enhancement of the critical current $J_c$ [4] as well as for

 

the overall superconducting behavior of the Pr-doped Y123 compounds [5–7].

Our previous studies on various (R1–R2)123 mixed rare-earth compounds have shown that atomic substitutions induce phase separation, which correlates with the relaxation of internal mismatch strains due to the difference in ionic radii of the specific elements [8]. Inhomogeneities in these mixed cuprates manifest themselves by the formation of presumably nanodomains rich in either R1 and/or R2 together with an intermediate phase [8–12]. In the homologous $Y_{1-x}La_xBa_2Cu_3O_y$ system, with the larger isovalent $La^{3+}$ replacing the smaller $Y^{3+}$, the deconvolution of the lineshape of the $B_{1g}$-like phonon associated with the out-of-phase vibrations of the plane oxygen atoms revealed the presence of two phases attributed to the compositional inhomogeneity at the La/Y site: an intermediate one $Y_{1-z}La_zBa_2Cu_3O_y$, with less than the nominal La concentration, and a pure La123 with apparently reduced $T_c$. The observed small reduction in $T_c$ in that system could be interpreted based on the formation of the La123 phase upon La doping. In addition, the formation of the La123 nanodomains has been found to correlate with microstructural characteristics such as the crystallite microstrains obtained from the broadening of the XRD diffraction peaks [10]. On the other hand, when $Ca^{2+}$, with almost the same ionic size as $La^{3+}$, substitutes for $Y^{3+}$ in Y123 cuprate, it has the tendency to be surrounded by Y atoms, forming an independent nanophase of the $Y_{0.5}Ca_{0.5}Ba_2Cu_3O_y$ type in a matrix of Y123 cells [11]. The curvature of the diamagnetic signal shows two maxima $T_c$ in that system [13] supporting the phase separation scheme.

The above results suggest that both the size and the valence of the substituting element play a role in the phase separation mechanism. Moreover, phase separation effects should be taken into account when interpreting superconducting properties in the solid solutions (R1–R2)123. As far as the ionic size is concerned, $Pr^{3+}$ has a comparable ionic radius to both $La^{3+}$ and $Ca^{2+}$. On the other hand, the question of the valence state of Pr in the Pr123 compound has been the subject of investigation for a long time [1]. It is now well accepted that most likely the true valence of Pr is +3 and the apparent valence is between +3.3 and +3.4 [14–16]. The latter could be attributed to the presence of strains, as discussed in the following sections, or to the strong covalent character of the Pr–O bond, as proposed by Cao *et al* [16]. Therefore the expected phase separation features in the (Y–Pr)123 solid solution may show some differences from those observed in the homologous systems (Y–La)123 and (Y–Ca)123 and their study can give a better insight in order to interpret the superconducting properties of the Pr-doped compounds. Our preliminary Raman study of the (Y–Pr)123 system suggested the development of three presumably nanoscopic phases, one pure Y123, one Pr123 together with a mixed Y–Pr123. In addition, an unexpected increase of the Ba phonon energy with increasing Pr content implied a possible substitution of Pr at the Ba site [12]. However, the XRD data obtained using a laboratory diffractometer did not contain sufficient information that could support our above initial conclusions.

In this work we present a systematic study of inhomogeneities, lattice distortions and microstructural features in $Y_{1-x}Pr_xBa_2Cu_3O_y$ ($x = 0.0$–$1.0$) polycrystalline compounds combining micro-Raman spectroscopy with high resolution synchrotron x-ray powder diffraction. Since phase separation effects, anticipated by micro-Raman spectroscopy, are expected to correlate with local lattice distortions and microstructural features, High Resolution Synchrotron Diffraction, where the instrumental contribution to diffraction line broadening is negligible, is the most appropriate tool to study lattice distortions and microstructure. The lineshape of the $B_{1g}$-like phonon mode of the plane oxygen atoms has been used as evidence for the development of locally different rare-earth nanoscopic environments (phases) upon Pr doping, which have been found to correlate with variations of local lattice distortions and crystallite microstrains obtained by diffraction pattern analysis. Additional information is provided by the spectral changes in the apical oxygen phonon mode of $A_g$-symmetry. Synchrotron x-ray powder diffraction profiles have shown that Pr substituting for Y and/or Ba acts as a source of crystal defects, the Pr123 phase being a strained phase compared to the Y123. Alterations of the Ba phonon energy have been found to correlate with $Pr_{Ba}$ antisite defects, increase of crystallite macrostrains, increase of uncorrelated local lattice distortions and the formation of a pure Pr123 phase.

## 2. Experimental details

Polycrystalline ceramic samples $Y_{1-x}Pr_xBa_2Cu_3O_y$ (nominal compositions corresponding to $x = 0.00$, 0.10, 0.15, 0.20, 0.25, 0.30, 0.35, 0.40, 0.45, 0.50, 0.55, 0.60, 0.70, 0.80, 0.90 and 1.00) and two $YBa_{2-z}Pr_zCu_3O_y$ ($z = 0.1$ and 0.20) have been synthesized from high purity (99.999%) powders $Y_2O_3$, $Pr_6O_{11}$, $BaCO_3$ and CuO by the solid-state reaction method. The starting materials have been mixed according to the nominal compositions, ground, pressed into tablets and calcinated at 920 °C for 33 h. The pellets have been reground, repressed and further thermally treated in air for 30 h at 950 °C and 960 °C, respectively. Sintering of the samples has been performed under flowing oxygen at 950 °C for 30 h. The samples have then been cooled down to 500 °C in the furnace and annealed at that temperature for 32 h under flowing oxygen. The process (sintering and annealing) has been repeated until the amount of the secondary phase $BaCuO_2$ was reduced as much as possible. The superconducting critical temperature has been determined using a SQUID magnetometer in the zero-field-cooled (ZFC) mode. Oxygen stoichiometry has been obtained by a volumetric method, taking into account the presence of the $BaCuO_2$ secondary phase for each sample [17].

The micro-Raman spectra have been acquired mainly at room temperature with a Jobin-Yvon T64000 triple spectrometer, equipped with a liquid-nitrogen-cooled CCD and a microprobe (objective lens magnification 100×), on individual micro-crystals (typical size of a few $\mu$m) in two scattering geometries: the incident and scattered light polarization were kept either along the $c$ axis ($zz$ polarization) or parallel to the $ab$ plane ($xx/yy$ polarization). Several laser lines (476.2 nm, 488.0 nm and 514.5 nm of an $Ar^+$ laser, 647.1 nm of a $Kr^+$ laser and 632.8 nm of an He–Ne laser) were

used for excitation, at a power of <0.2 mW focused on a 1–2 $\mu$m diameter spot size. Accumulation times were 1 and 2 h for the $zz$ and $xx/yy$ scattering geometries, respectively.

Synchrotron x-ray powder diffraction patterns were collected at two high resolution beamlines, BM01B ($\lambda$ = 0.600 08 Å, $T$ = 15 K) and ID31 ($\lambda$ = 0.500 11 Å, RT) of ESRF, Grenoble, France. The experimental set-up is described in detail elsewhere (BM01B [18] and ID31 [19]). The short wavelengths, to reduce absorption, were selected with a double-crystal Si(111) monochromator and calibrated with Si NIST ($a$ = 5.430 94 Å). Optimum transmission was achieved by enclosing the finely ground samples in 0.7 mm diameter borosilicate glass capillaries and appropriate spinning of the capillaries in the beam ensured a good powder averaging. Data were rebinned in the $2\theta$ range 0.52°–45.5° in steps of 0.004°. The patterns at 15 K were recorded by placing the capillary in an exchange gas continuous liquid-helium-flow cryostat (Cryovac-KONTI) with rotating sample rod.

## 3. Results

### *3.1. High resolution synchrotron x-ray diffraction*

The XRD patterns have been analyzed with the Rietveld method using the GSAS software package [20], taking into account two phases for each sample, the main (Y–Pr)123 and the secondary phase $BaCuO_2$. The refinements were carried out using, for the (Y–Pr)123 phase, the starting crystal structure model of Y123 [21] (space group $Pmmm$) and for the $BaCuO_2$ the starting structural parameters reported in [22]. The peak profile was described by a pseudo-Voigt function corrected for asymmetry and axial divergence [23]. For the data measured at 15 K it was possible to refine the isotropic atomic displacement factors for all atoms. Pr was allowed to occupy both the 1h(1/2, 1/2, 1/2) Y site as well as the 2t(1/2, 1/2, $z$) Ba site. The refinement of a mixed Ba/Pr occupation factor at 15 K was stable in spite of the poor x-ray contrast for the two elements, leading to reasonable values of the Pr occupancies, as will be discussed in the following section. Figure 1 shows the results of Rietveld refinement at 15 K for the two end member compounds Y123 (figure 1(a)) and Pr123 (figure 1(b)). The calculated intensities describe very well the observed pattern of Y123, but do not reproduce details of the profile for certain reflections of Pr123, as described below. The high resolution diffraction data have shown that any phase separation effects, as were anticipated by Raman spectroscopy in the mixed (Y–Pr)123 phase, are not evident on a macroscopic scale since no Bragg peaks which belong to the pure Y123 or Pr123 phase are present at any of the intermediate compositions. This is shown in the inset of figure 1, where a characteristic part of the experimental pattern, near the 020, 006 and 200 reflections, of the $x$ = 0.45 compound is compared with that of the Pr123 phase. On the other hand, anisotropic broadening of Bragg peaks is evident (inset of figure 1), which has been modeled in the refinement with the microstrain description of Stephens [24] (profile no. 4 in GSAS).

Table 1 presents the refined structural parameters of the (Y–Pr)123 compounds at 15 K, the impurity phase $BaCuO_2$ content and the Pr occupancy at the Ba site $n$ ($Pr_{Ba}$). It also shows the measured oxygen content ($y$). All samples were optimally doped or overdoped ($y$ = 6.91–7.04).

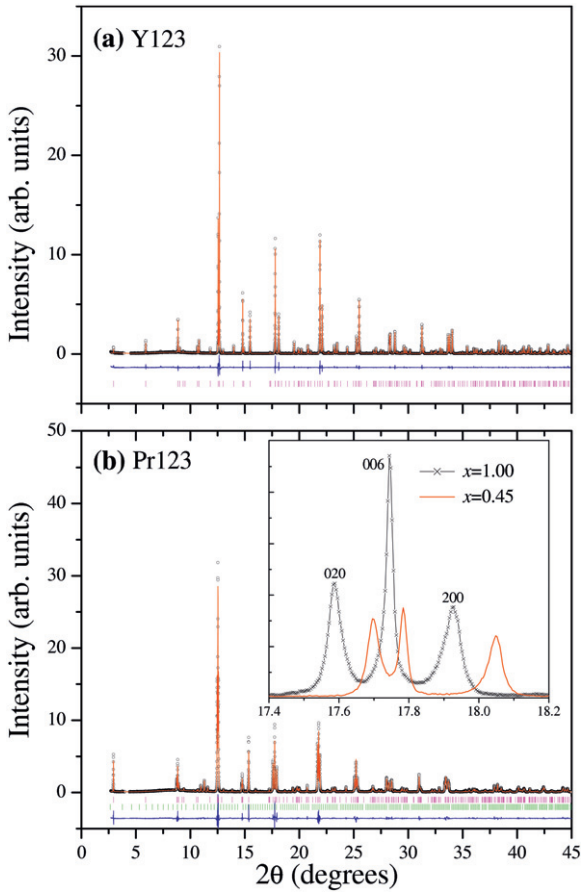


**Figure 1.** Experimental (circles) and calculated (continuous line) synchrotron x-ray powder diffraction patterns at 15 K, as well as their difference (bottom line), for the two end member compounds Y123 ($x$ = 0.00) (a) and Pr123 ($x$ = 1.00) (b). Bars show the Bragg positions of Y123 (a) and Pr123 as well as $BaCuO_2$ (b) phases. The inset shows the experimental pattern near the 020, 006 and 200 reflections of the $x$ = 0.45 compound in comparison with that of the Pr123 phase ($x$ = 1.00).

*Average structure of the (Y–Pr)123 compounds*

The average amount of Pr in the Y site obtained from the Rietveld analysis coincides with the nominal composition except for samples with nominal $x$ = 0.9 and 1.0 where the refined values are 0.85 and 0.93, respectively, indicating the presence of Pr vacancies. The occupancy of Pr atoms, allowed to enter the Ba site ($Pr_{Ba}$ antisite defects), has been refined separately at the final steps of analysis. The amount (% per Ba site) of these defects has been found to increase with Pr content reaching a value of 12.7% for the end compound Pr123. The substitution of Pr at the Ba site is evident by the presence of the secondary phase $BaCuO_2$ (table 1). Convincing evidence that an increased amount of Ba is occupied by Pr has been obtained from our previous preliminary Raman investigations [12] and will be discussed in what follows.

**Table 1.** Rietveld refinements of XRD data for $Y_{1-x}Pr_xBa_2Cu_3O_y$. The space group is *Pmmm* with Ba($\frac{1}{2}$, $\frac{1}{2}$, *z*), Pr($\frac{1}{2}$, $\frac{1}{2}$, $\frac{1}{2}$), Y($\frac{1}{2}$, $\frac{1}{2}$, $\frac{1}{2}$), Cu1(0, 0, 0), Cu2(0, 0, *z*), O1(0, 0, *z*), O2(0, $\frac{1}{2}$, *z*), O3($\frac{1}{2}$, 0, *z*) and O4(0, $\frac{1}{2}$,0). The measured oxygen content *y* is also shown.

| | $x = 0.00$ | $x = 0.20$ | $x = 0.30$ | $x = 0.45$ | $x = 0.60$ | $x = 0.80$ | $x = 0.90$ | $x = 1.00$ |
|---|---|---|---|---|---|---|---|---|
| *z* (Ba) | 0.183 58(4) | 0.182 81(5) | 0.182 76(5) | 0.182 16(5) | 0.181 70(5) | 0.181 11(6) | 0.1805(1) | 0.180 32(6) |
| *z* (Cu2) | 0.354 39(9) | 0.353 68(9) | 0.3531(1) | 0.3525(1) | 0.3514(1) | 0.3511(1) | 0.3450(3) | 0.3495(1) |
| *z* (O1) | 0.1595(5) | 0.1627(5) | 0.1596(6) | 0.1628(6) | 0.1617(6) | 0.1597(7) | 0.1614(7) | 0.1638(6) |
| *z* (O2) | 0.3792(5) | 0.3777(5) | 0.3769(6) | 0.3756(5) | 0.3759(6) | 0.3758(6) | 0.3715(7) | 0.3707(6) |
| *z* (O3) | 0.3811(5) | 0.3781(5) | 0.3798(5) | 0.3783(5) | 0.3768(5) | 0.3767(6) | 0.3729(7) | 0.3732(6) |
| *a* (Å) | 3.810 66(1) | 3.817 12(2) | 3.822 16(3) | 3.826 09(2) | 3.834 09(3) | 3.840 31(2) | 3.846 90(2) | 3.852 07(2) |
| *b* (Å) | 3.881 09(1) | 3.891 47(2) | 3.893 88(2) | 3.899 96(2) | 3.906 03(2) | 3.915 39(2) | 3.919 29(2) | 3.923 66(2) |
| *c* (Å) | 11.638 86(3) | 11.640 10(5) | 11.637 27(6) | 11.645 18(5) | 11.649 32(7) | 11.653 62(6) | 11.661 56(6) | 11.670 18(6) |
| $R_p$ | 0.0856 | 0.0865 | 0.1047 | 0.0806 | 0.0888 | 0.1018 | 0.0885 | 0.0933 |
| $R_{wp}$ | 0.1221 | 0.1178 | 0.1462 | 0.1117 | 0.1201 | 0.1379 | 0.1173 | 0.1242 |
| $R(F^2)$ | 0.0324 | 0.0559 | 0.0604 | 0.064 | 0.065 | 0.0662 | 0.0612 | 0.0645 |
| *n* ($Pr_{Ba}$) | 0.000 | 0.020 | 0.055 | 0.010 | 0.036 | 0.066 | 0.088 | 0.127 |
| $BaCuO_2$ (%) | — | 1.00 | 4.42 | 3.98 | 6.71 | 7.88 | 9.74 | 9.36 |
| *y* | 7.00(1) | 6.96(1) | 6.987(8) | 6.959(8) | 6.91(2) | 6.95(1) | 6.925(8) | 6.92(2) |

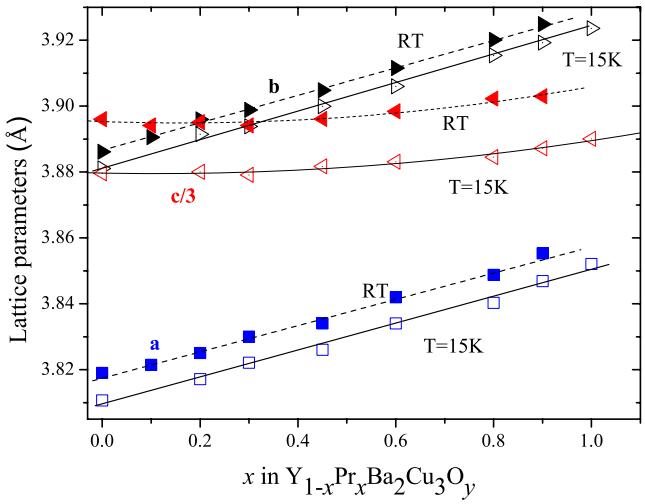


**Figure 2.** Dependence of the *a*, *b* and *c*/3 lattice parameters at 15 K (open symbols) and at room temperature (full symbols) of the (Y–Pr)123 compounds on the Pr content *x*. Solid lines (dashed lines) are fits of the data for 15 K (RT) with first-or second-order polynomials.

The lattice constants and unit cell volume increase with the nominal Pr content *x*, in accordance with the larger $Pr^{3+}$ ($r = 1.126$ Å) replacing the smaller $Y^{3+}$ ($r = 1.019$ Å) in the 1h(1/2, 1/2, 1/2) site in the center of the unit cell (figure 2). However, unlike the case of the homologous (Y–La)123 system [10], the internal pressure induced by the larger $Pr^{3+}$ ion results in a quite anisotropic strain: the *a* and *b* axes increase linearly with Pr content *x* (by 1.08% at 15 K) while the *c* axis, remaining almost constant for $0 < x < 0.6$, increases only by 0.27% for Pr123. In (Y–La)123 the increase of lattice parameters with La content was found to be almost isotropic [10]. The orthorhombic strain, defined as $(b - a)/(b + a)$, does not change through all the compositional range. In the (Y–La)123 system [10], with La having a comparable ionic radius to Pr, we have found that orthorhombic strain decreases (up to a value of 50%) with increasing amount of La substitution. Figure 2 shows that thermal expansion is anisotropic, with the *c* lattice constant exhibiting the largest expansion and the *b* axis the smallest in agreement with earlier studies on the Y123 compound [25, 26]. This can be understood taking into account that the *b* axis is the most rigid one in the structure due to the presence of chain oxygen $O_{ch}$ and the *c* axis is the less rigid due to the lack of oxygens on the Y/Pr plane. Thermal expansion seems not to depend on the Pr content *x*.

Individual bond lengths (table 2) have been calculated with the oxygen atoms labeled as follows: O1 apical, O2 and O3 plane ($O_{pl}$) along the *b* and *a* axes, respectively, and O4 chain ($O_{ch}$) along the *b* axis. The Cu2–Cu2 distance is monotonically increasing while the corresponding Cu2–Cu1 is decreasing with Pr doping (figure 3(a)) as a consequence of the bigger Pr replacing the smaller Y atom in the central cube of the triple-perovskite unit cell. In order to estimate the ionic size effect of the substituting atoms on the *c*-axis expansion, we compare the changes of the bonds along the *c* axis (at room temperature) in the two homologous compounds $Y_{1-x}Pr_xBa_2Cu_3O_y$ and $Y_{1-x}La_xBa_2Cu_3O_y$ [10]. The change of the Cu2–Cu2 (Cu1–Cu2) distance for a given change $\Delta\overline{r}$ of the average ionic radius (Y–Pr and Y–La, respectively) normalized to the corresponding value at $x = 0$ is $64.8 \times 10^{-2}$ ($-14.4 \times 10^{-2}$) in the La-doped and $44.3 \times 10^{-2}$ ($-14.5 \times 10^{-2}$) in the Pr-doped compounds, respectively. The increase of the Cu2–Cu2 bond distance in the Pr123 compound does not follow the ionic size trend, e.g. the value of the Cu2–Cu2 distance is smaller than expected [27]. On the other hand, the decrease of the Cu1–Cu2 distance in Pr123 is similar to that of La123. Considering the triple-perovskite structure of the Y123 family, the Cu1–Cu2 distance decrease is mainly a consequence of the compressive stress that is imposed on the perovskite block hosting the Ba atom by the larger Pr (or La) substituting for the smaller Y, and of the corresponding increase of the Cu2–Cu2 distance. Since the latter has been found significantly smaller in Pr123 compared to La123, one would also expect that the Cu1–Cu2 distance decrease in Pr123 would be correspondingly smaller in Pr123 compared to La123, contrary to the above results. This implies that an additional effect, besides the increase of the Cu2–Cu2 distance due to Pr substitution at the Y site, accounts for the decrease of

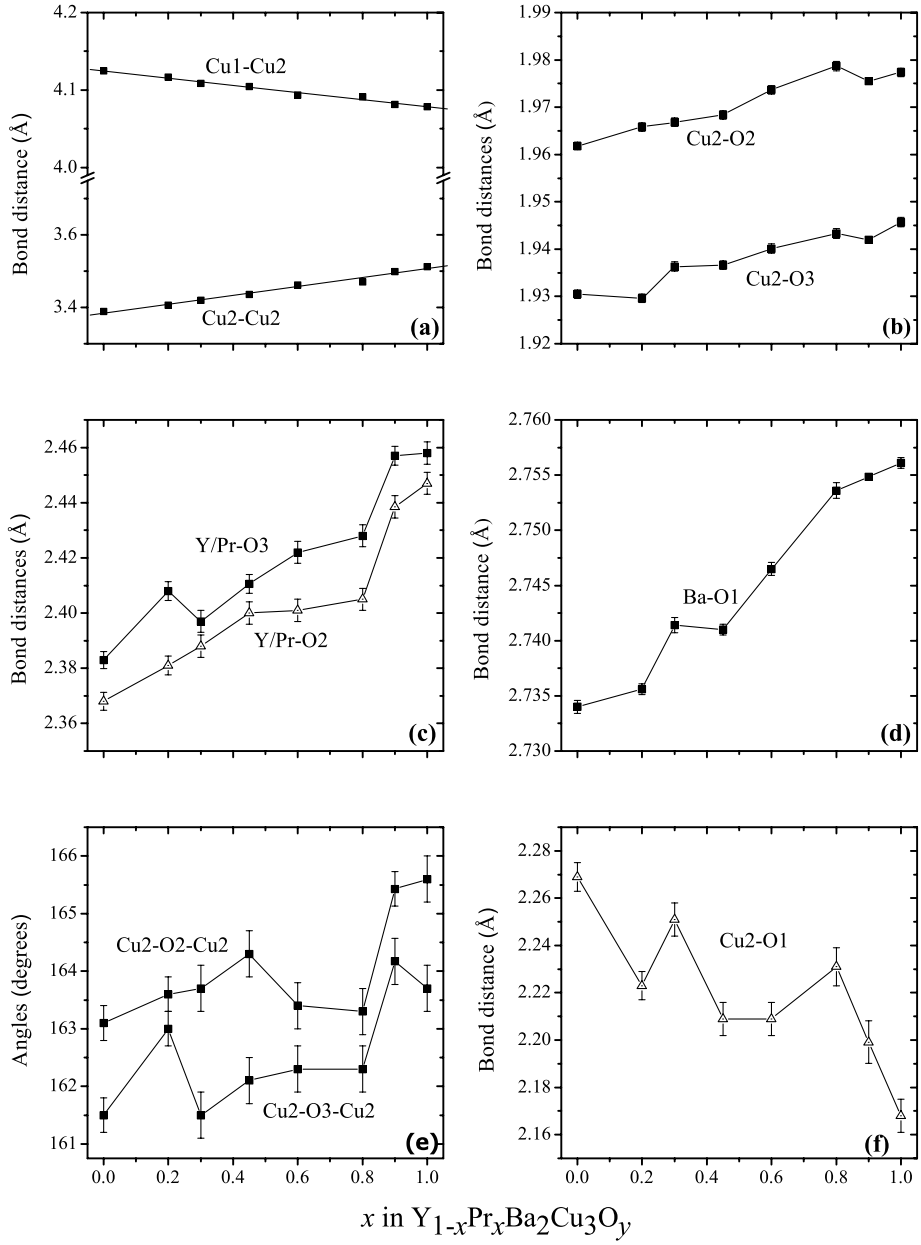


**Figure 3.** Dependence of the bond distances Cu2–Cu2, Cu1–Cu2 (a), Cu2–O2, Cu2–O3 (b), Y/Pr–O2, Y/Pr–O3 (c), Ba–O1 (d), angle Cu2–O2–Cu2, Cu2–O3–Cu2 (e) and bond distance Cu2–O1 (f) at 15 K of the (Y–Pr)123 compounds on the Pr content $x$.

the Cu1–Cu2 distance in the Pr123 compound. This additional effect is most likely the partial substitution of the smaller Pr for the bigger Ba, as evidenced by the Rietveld analysis and Raman investigations. The changes of both Cu2–Cu2 and Cu1–Cu2 bond distances indicate that the observed very small increase of the $c$ lattice constant upon Pr doping (figure 2) is a synergetic effect of both, a smaller than expected increase of Cu2–Cu2 distance by the ionic size effect and an additional decrease of the Cu1–Cu2 distance, due to the $Pr_{Ba}$ antisite defects.

The Cu2–$O_{pl}$ (figure 3(b)), the Y/Pr–$O_{pl}$ (figure 3(c)) and the Ba–O1 (figure 3(d)) bond lengths have an overall increasing tendency with Pr content $x$, following the corresponding increase of the $a$ and $b$ lattice parameters. Modifications at Pr content $x \approx 0.2$ and $x \approx 0.8$ are observed in the Y/Pr–O3 and Cu2–O3 bond lengths and in the corresponding Cu2–O3–Cu2 angle values (figure 3(e)). After an initial increase, the internal strain of the Y/Pr–O3, Cu2–O3 bonds partially relaxes at $x > 0.2$ and for $x > 0.8$ enhanced values are evidenced. The average Pr–$O_{pl}$ bond distance for the Pr123 compound has been found to be shorter (2.4525 Å) than expected according to the ionic radius trend (2.48 Å) [27]. The Cu2–O3–Cu2 angle for Pr123 is quite small (163.7°) and the average Cu2–$O_{pl}$–Cu2 angle is also smaller than that expected by the ionic radius trend [27]. The Cu2–O1 bond decreases with Pr content $x$ (figure 3(f)). It is worth mentioning that no remarkable change is observed at the critical composition $x = 0.6$ in all bond lengths obtained from the average structure.

Figure 4 illustrates the isotropic atomic displacement parameters $U_{iso}$ of the Cu, Y/Pr and Ba atoms obtained from

**Table 2.** Bond lengths (Å) of the $Y_{1-x}Pr_xBa_2Cu_3O_y$ orthorhombic compounds.

| | $x = 0.00$ | $x = 0.20$ | $x = 0.30$ | $x = 0.45$ | $x = 0.60$ | $x = 0.80$ | $x = 0.90$ | $x = 1.00$ |
|---|---|---|---|---|---|---|---|---|
| Y/Pr–O2 × 4 | 2.368(3) | 2.381(3) | 2.388(4) | 2.400(4) | 2.401(4) | 2.405(4) | 2.438 54(1) | 2.447(4) |
| Y/Pr–O3 × 4 | 2.384(3) | 2.408(3) | 2.397(4) | 2.411(3) | 2.423(4) | 2.428(4) | 2.457 01(1) | 2.458(4) |
| Ba–O1 × 4 | 2.7340(6) | 2.7355(5) | 2.7415(7) | 2.7410(5) | 2.7465(6) | 2.7535(7) | 2.754 87(1) | 2.7560(5) |
| Ba–O2 × 2 | 2.969(4) | 2.965(4) | 2.959(5) | 2.955(5) | 2.965(5) | 2.972(5) | 2.942 89(1) | 2.940(5) |
| Ba–O3 × 2 | 3.008(4) | 2.992(4) | 3.008(5) | 3.003(4) | 2.997(5) | 3.005(5) | 2.979 31(1) | 2.986(5) |
| Ba–O4 × 2 | 2.8628(4) | 2.8585(4) | 2.8593(4) | 2.8565(4) | 2.8557(5) | 2.8534(5) | 2.851 09(1) | 2.8527(5) |
| Cu1–O1 × 2 | 1.856(6) | 1.894(6) | 1.857(7) | 1.896(7) | 1.884(7) | 1.861(8) | 1.882 23(1) | 1.912(7) |
| Cu1–O4 × 2 | 1.940 54(1) | 1.945 73(1) | 1.946 94(1) | 1.949 98(1) | 1.953 02(1) | 1.957 70(1) | 1.959 64(1) | 1.961 83(1) |
| Cu2–O1 × 1 | 2.269(6) | 2.223(6) | 2.252(7) | 2.209(7) | 2.210(7) | 2.231(8) | 2.199 09(1) | 2.167(7) |
| Cu2–O2 × 2 | 1.9619(8) | 1.9657(8) | 1.9666(9) | 1.9684(8) | 1.9737(9) | 1.979(1) | 1.975 59(1) | 1.9773(9) |
| Cu2–O3 × 2 | 1.9305(9) | 1.9296(8) | 1.9363(1) | 1.9365(9) | 1.940(1) | 1.943(1) | 1.941 94(1) | 1.946(1) |
| Cu1–Cu2 | 4.158(7) | 4.164(8) | 4.141(7) | 4.134(7) | 4.12(1) | 4.12(1) | 4.12(1) | 4.10(1) |
| Cu2–Cu2 | 3.36(1) | 3.35(1) | 3.41(1) | 3.43(1) | 3.50(2) | 3.48(2) | 3.50(2) | 3.58(2) |

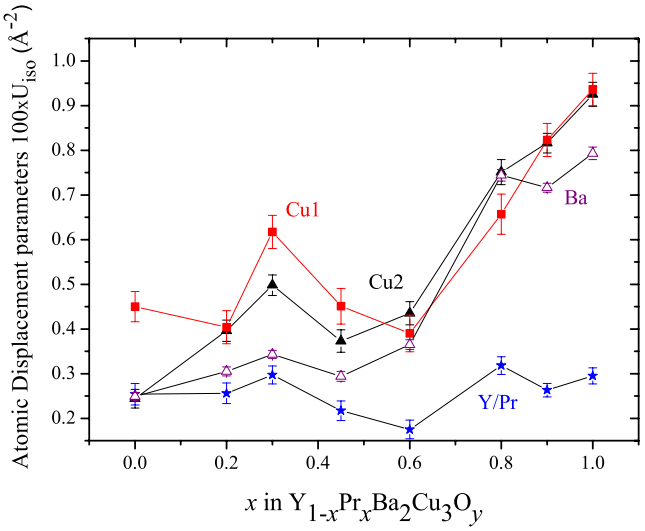


**Figure 4.** Variation of the isotropic atomic displacement parameters $U_{iso}$ of Cu1 (full squares), Cu2 (full triangles), Y/Pr (stars) and Ba atoms (open triangles) in the (Y–Pr)123 compounds with the Pr content $x$.

the refinement of the data at 15 K. Correlations among different parameters during the least-squares procedure may result in inaccurate values. In order to minimize this problem, we retain the same refinement conditions (i.e. number of refinables, background and profile coefficients). Therefore, we are able to follow the variation of $U_{iso}$ upon Pr doping, which can provide valuable qualitative information about the presence of local distortions (random displacements from the ideal atom positions). For $x > 0.6$ considerably increased values of $U_{iso}$ have been obtained for the Cu1 and Cu2 atoms as well as for the Ba atom while for the Y atom they are almost constant. This indicates that for $x > 0.6$ uncorrelated local lattice distortions are present in the cube of the triple-perovskite unit cell hosting the Ba atom. We have also performed refinements using anisotropic atomic displacement factors which resulted in equally good agreement $R$ factors to those using isotropic displacements. The refinements have shown that the Y/Pr, Ba and Cu2 atoms exhibit almost isotropic displacements with $U_{11} \approx U_{22} \approx U_{33}$. On the other hand, for the Cu1 atom the $U_{33}$ factors were almost two to three times smaller than the in-plane displacements, indicating that the Cu1 atom exhibits anisotropic lattice distortions mainly on the $ab$ plane.

*BVS analysis*

In order to have a better insight into the charge distribution and internal strain in the structure, we have used the bond valence sum (BVS) method introduced by Altermatt and Brown [28]. We have used the refined bond lengths at 15 K, after correcting the values to room temperature, to calculate the oxidation state of the Ba, Y/Pr, Cu1, Cu2, O2 and O3 atoms according to the relation $V_i = \sum \exp[(R_0 - R_{ij})/B]$, where $B = 0.37$ Å and $R_{ij}$ are the neighboring cation–anion distances. For each atom A participating in an A–O bond the corresponding bond valence parameter $R_0$ depends on the individual atom A and its initial assumed oxidation state. The oxidation state of Pr has been assumed to be +3 [14–16]. $R_0$ was set equal to 2.285 Å, 2.019 Å and 2.138 Å for $Ba^{2+}$, $Y^{3+}$ and $Pr^{3+}$, respectively [29, 30]. For $Cu^{1+}$, $Cu^{2+}$ and $Cu^{3+}$ was set equal to 1.6 Å, 1.679 Å and 1.739 Å, respectively [29]. For those sites in the structure exhibiting a mixed occupation, weighted values for the $R_0$ constant have been used according to the refined occupation values. For the Cu1, Cu2 atoms we have calculated the true $V_{Cu1}$ and $V_{Cu2}$ values, e.g. corrected for internal strain, following the procedure described in [29] and [31] in two steps: first, the values of the apparent oxidation state $V_{Cu1}^{ap}$ and $V_{Cu2}^{ap}$ have been calculated assuming the presence of both $Cu^{2+}$ and $Cu^{3+}$ according to equation (2) in [29]. Then, the mean calculated apparent $V_{Cu}^{ap}$ value for the Cu atoms in the unit cell has been compared to that expected by the stoichiometry. For each sample we have taken into account the measured oxygen content $y$. The difference between the value expected by stoichiometry and the experimental value is the correction due to strain. This difference has been added (or subtracted) to the apparent $V_{Cu1}^{ap}$ and $V_{Cu2}^{ap}$ values to obtain the 'true' oxidation state $V_{Cu1}$ and $V_{Cu2}$, respectively. This procedure assumes that the influence of internal strain is the same at both Cu1 and Cu2 atoms [31]. The bond valence sums for the O2 ($V_{O2}$) and for the O3 ($V_{O3}$) atoms have then been calculated using a weighted average for the $R_0$ parameter taking into account the strain corrected true valence, $V_{Cu2}$, of the Cu2 atom. Table 3 presents the average valence of the Cu atoms in the unit cell calculated from the 'true' bond valence

**Table 3.** Average valence of the Cu atoms $V_{Cu}^{a}$ calculated from XRD bond valence sums and $V_{Cu}^{b}$ expected from the variations in the concentration of oxygen ($y$), bond valence sums of plane oxygen atoms, number of holes $p$ in the $CuO_2$ plane and parameter $V_+$ according to [32] in the $Y_{1-x}Pr_xBa_2Cu_3O_y$ compounds.

| $x$ | $V_{Cu}^{a}$ | $V_{Cu}^{b}$ | $V_{O2}$ | $V_{O3}$ | $p$ | $V_+$ |
|---|---|---|---|---|---|---|
| 0.00 | 2.330 | 2.333 | 2.047 | 2.063 | 0.219 | −0.440 |
| 0.20 | 2.252 | 2.307 | 2.068 | 2.084 | 0.210 | −0.514 |
| 0.30 | 2.299 | 2.325 | 2.071 | 2.087 | 0.141 | −0.457 |
| 0.45 | 2.255 | 2.306 | 2.088 | 2.104 | 0.142 | −0.526 |
| 0.60 | 2.244 | 2.273 | 2.097 | 2.106 | 0.093 | −0.499 |
| 0.80 | 2.238 | 2.300 | 2.116 | 2.121 | 0.003 | −0.477 |
| 0.90 | 2.235 | 2.283 | 2.107 | 2.116 | 0.068 | −0.515 |
| 1.00 | 2.234 | 2.280 | 2.115 | 2.125 | 0.064 | −0.543 |

sums $V_{Cu1}$ and $V_{Cu2}$ together with the values expected from the variations of the oxygen concentration ($y$) and the bond valence sums of the plane oxygen atoms O2($V_{O2}$) and O3($V_{O3}$). The average valence of the copper atoms has been found to decrease with Pr content.

The number of holes $p$ per Cu2 atom on the $CuO_2$ planes, also presented in table 3, have been calculated from the sum of excess copper and oxygen charge according to the relation $p \approx V_- = [2 + V_{Cu2} - V_{O2} - V_{O3}]$ [32] where $V_{Cu2}$, $V_{O2}$ and $V_{O3}$ are the bond valence sums calculated from XRD data at the Cu2, O2 and O3 sites, respectively. A drastic decrease of the number of holes is observed with increasing Pr content. According to Tallon [33] the scaled transition temperature $T_c/T_{c,max}$ seems to be a universal, approximately parabolic, function of hole concentration which has its onset, maximum and termination at $p \approx 0.05$, 0.16 and 0.27, respectively. For the samples with Pr content $x = 0.8$, 0.9 and 1.0 we have obtained a value of $p$ close to or well below the threshold for onset of $T_c/T_{c,max}$ (0.05). On the other hand, the sample with $x = 0.6$ with $T_c = 0$ and $p = 0.91$ does not follow this prediction. The distribution of holes between copper and oxygen atoms can be estimated from the parameter $V_+ = [6 - V_{Cu2} - V_{O2} - V_{O3}]$ as proposed by Tallon [32]. The values of $V_+$ (table 3) suggest that the holes are localized at the Cu sites [32].

For the Ba and Y/Pr sites the excess valence, e.g. the difference between the experimental valence sums and the expected oxidation state (2+ and 3+ for Ba and Y/Pr, respectively), is a measure of the internal strain in the structure. Figure 5 shows that excess valence at the Y site in the overdoped Y123 ($x = 0.0$) sample is about −0.06 valence units (v.u.) [29] so that the Y atom is under a small tensile stress. At $x > 0.2$ excess valence becomes positive and hence the strain becomes compressive, increasing with Pr content $x$. This is a consequence of the bigger Pr substituting for the smaller Y. For $x > 0.8$ the internal strain is partially relieved. This can be understood taking into account the presence of Pr vacancies obtained by the Rietveld refinement for the samples $x = 0.9$ and 1.0. At the Ba site a value of ≈0.18 v.u. of excess valence has been obtained for $0.0 \leqslant x < 0.6$, which indicates the presence of a compressive stress on the Ba atom (figure 5). Our samples are optimally doped or overdoped so the above results are in agreement with the results presented in [29] for the internal strain dependence on the oxygen content in the Y123 compounds. The decrease of excess valence and hence the partial relief of compressive strain observed for $x \geqslant 0.6$ is a result of the apparent partial substitution of the smaller Pr ion for the bigger Ba.

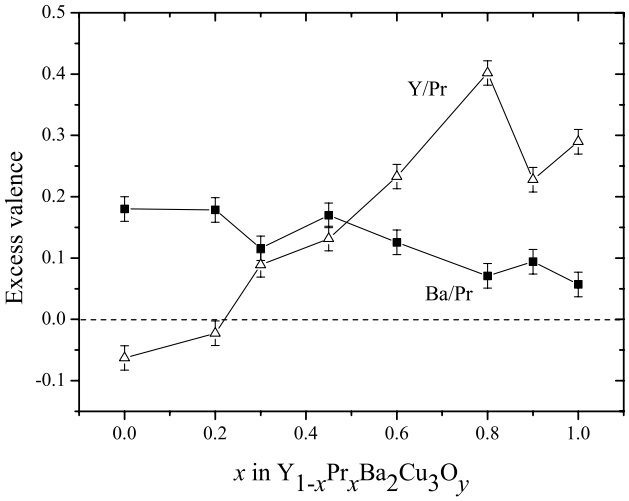


**Figure 5.** The internal strain expressed as the difference between the bond valence sums and the expected oxidation states at the Y and Ba sites in the (Y–Pr)123 compounds as a function of the Pr content $x$.

*Microstructure*

In order to assess the microstructural characteristics directly from the observed peak widths, Williamson–Hall plots [34] were constructed. We have found that both size-type and anisotropic microstrain-type peak broadening are present. Since we investigated the evolution of the size of the coherently diffracting domains and the microstrains on Pr doping rather than their absolute values, the instrumental effect has been assumed to be negligibly small. The size of the presumably spherical coherently diffracting domains has been estimated from the Scherrer formula $P(\mu m) = (180/\pi)\ (K\lambda/100L_x)$, where $K = 0.9$ is the Scherrer constant, $\lambda$ the wavelength and $L_x$ the refined Lorentzian coefficient for the size-type broadening [20]. Figure 6(a) shows the variation of the average size of the diffracting domains P upon Pr content $x$. Data collected at two beamlines and two different temperatures (BM01B at 15 K and ID31 at RT) are employed, showing a very good agreement and reproducibility. The average size of diffracting domains is reduced when Pr substitutes for Y in the Y123 compounds, showing minimum values for the intermediate compositions $0.2 < x \leqslant 0.8$.

The anisotropic microstrain broadening has been modeled with the description of Stephens [24], which is incorporated into GSAS. Microstrain-type broadening in this model is considered as a manifestation of the distribution of the metric parameters of the reciprocal lattice. A distribution of lattice parameters can originate from crystalline defects or local inhomogeneities of chemical composition. The microstrain along the direction $[hkl]$ has been calculated from the relation [20]:

$$\frac{\delta d_{hkl}}{d_{hkl}} = \pi[\sigma^2(M_{hkl}]^{1/2}/(18\,000M_{hkl}) \qquad (1)$$

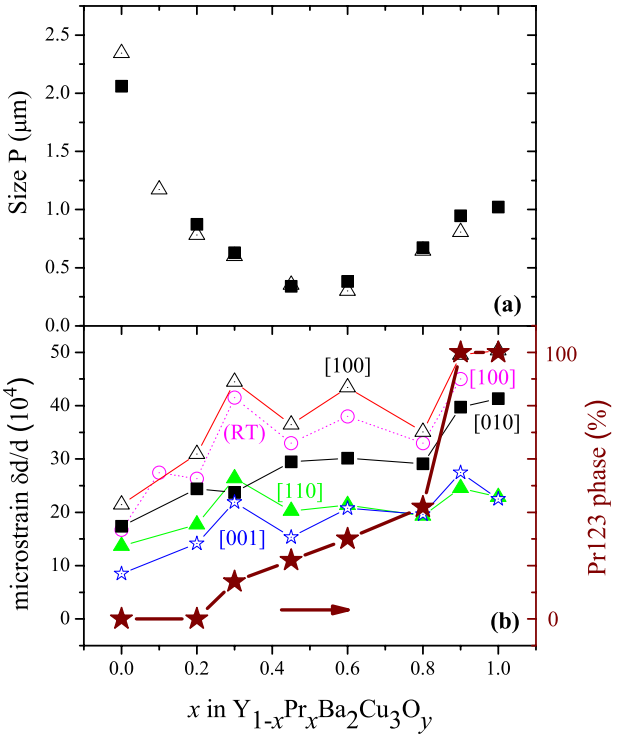


**Figure 6.** (a) Variation of the average size of the diffracting domains upon Pr content $x$. Full squares and open triangles are values obtained from patterns collected at 15 K on BM01B with $\lambda = 0.600\,08$ Å and at RT on ID31 with $\lambda = 0.500\,11$ Å, respectively. (b) Variation of microstrains along different directions as a function of Pr content $x$. Open circles are microstrains along [100] calculated from the line broadening at RT. Besides, the relative amount of the Pr123 phase induced by the deconvolution of the $B_{1g}$-symmetry Raman-active band is shown by filled stars.

where $M_{hkl} = 1/d^2_{hkl}$ and $\sigma^2(M_{hkl})$ is the variance of $M_{hkl}$, which determines the strain-broadening contribution to the width of the diffraction line $hkl$. For an orthorhombic structure $\sigma^2(M_{hkl})$, and the diffraction width, is parameterized with six refinable coefficients, $S_{HKL}$, as

$$\sigma^2(M_{hkl}) = S_{400}h^4 + S_{040}k^4 + S_{004}l^4 + 3(S_{220}h^2k^2 + S_{202}h^2l^2 + S_{022}k^2l^2). \quad (2)$$

Negative values for the $S_{220}$ coefficient have been obtained, indicating a negative correlation between the variation of $a$ and $b$ lattice parameters. The refined values of the $S_{004}$ coefficient are, for all samples, two to three orders of magnitude smaller than the corresponding $S_{400}$ and $S_{040}$, indicating anisotropy of microstrains. Anisotropic microstrains constitute a common feature in different high $T_c$ cuprates, such as $La_{1.85}A_{0.15}CuO_4$ (A = Sr, Ba, Ca) and Bi–Cu–O compounds [35]. The variation of microstrains along the [100], [010], [001] and [110] directions as a function of the Pr content is shown in figure 6(b). Microstrains are minimum along the [001] and [110] directions and maximum along the [100] direction, e.g. perpendicular to the chains. For comparison, the microstrain along the [100] direction calculated from the line broadening at RT is also shown, as well as the relative amount of the Pr123 phase induced by the deconvolution of the $B_{1g}$-symmetry Raman-active band discussed below. The microstrain pattern is the same both at RT and at 15 K, indicating that its origin is not a temperature-driven effect. Structural defects, such as dislocations and stacking faults lying in the $ab$ plane, are most likely the origin of the observed large anisotropic strains. In Y123 powders subjected to different levels of stress, edge or mixed type dislocations were always observed to lie on the (001) plane [36]. Such dislocations can induce microstrains and enhanced broadening of the $h00$ reflections. In addition, high temperature annealing of the Y123 [36] or the presence of local compositional fluctuations [37–39] result in the formation of extrinsic stacking faults with an intercalation of an extra CuO layer, offsetting the Ba atom by half a unit cell in the $b$ or $a$ axis direction.

Owing to the negligible instrumental contribution to broadening, the diffraction profiles measured at a synchrotron high resolution diffractometer can reveal even subtle microstructural features of the investigated samples. The calculated Bragg scattering intensities, modeled with anisotropic strain-type and isotropic size-type broadening effects, describe very well the experimental peak profiles for the compounds with $x \leqslant 0.2$. However, with increasing Pr substitution ($x \geqslant 0.3$), details of the peak profile for specific reflections cannot be reproduced very well by the calculated intensities as shown in figure 7. The $hhl$ experimental reflections are narrower than the calculated ones, indicating a longer range of structural coherence along the diffraction vector $hhl$ compared to other directions. A small peak shift of the $h00$ reflections is observed which increases with diffraction order. Orthorhombic double peak groups of the form $hkl$ and $khl$ exhibit asymmetric tails as well as excess intensity in-between. The above observations apply to the diffraction profiles measured both at 15 K as well as at RT, indicating again that their origin is not a temperature-driven effect. These features of the diffraction peak profile can originate from planar defects, e.g. stacking faults and twins, deteriorating structural coherence in specific directions, as shown in the case of fcc [40] and hexagonal crystals [41]. In the present study we have not attempted to model the specific planar defects due to the presence of peak overlapping in the diffraction pattern, which results from the complicated structure of Y/Pr123 and from the presence of the secondary phase $BaCuO_2$. Nevertheless some qualitative estimations can be drawn by the inspection of the above details of the profile. For instance, the peak shift of the $h00$ reflections, the asymmetric tails and excess intensity may indicate the presence of stacking faults. In this context, the increased local lattice disorder in the structure shown from the increasing values of the refined displacement factors for the Cu and Ba atoms (figure 4) may also reflect the presence of the above-mentioned stacking faults. On the other hand, the observed narrower $hhl$ peaks, and hence longer structural coherence along the diffraction vector $hhl$, is consistent with the presence of (110) microtwinning in the crystallites. Similar observations, assigned to (110) microtwinning, have been reported in Y123 powder samples investigated with high resolution neutron [42] and high resolution synchrotron diffraction [43]. In strained Y123 powders TEM observations

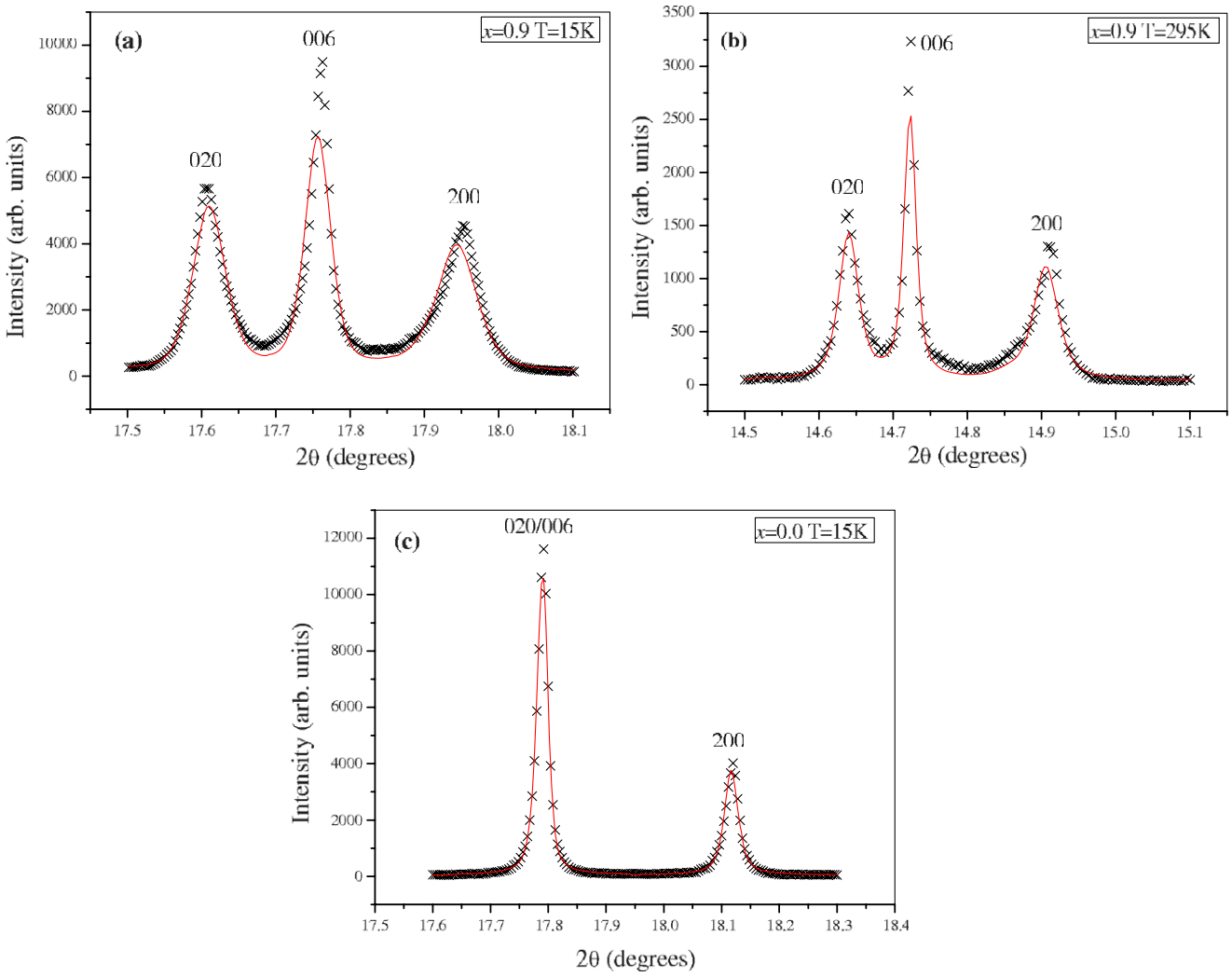


**Figure 7.** Experimental (cross symbols) and calculated (continuous line) synchrotron x-ray powder diffraction patterns near the 020, 006 and 200 reflections for the $Y_{0.1}Pr_{0.9}Ba_2Cu_3O_{6.92}$ compound at 15 K (a), at RT (b) and for the Y123 compound at 15 K (c).

have shown that small amounts of strain can be accommodated by deformation twinning on the {110} planes [36]. The above features are more pronounced with increasing Pr substitution in our samples so we estimate that the density of twins and stacking faults increase for $x > 0.2$. The reduced size of the coherently diffracting domains in the Pr-substituted samples compared to the Y123 phase supports the presence of planar defects in the former. The microstrains shown in figure 6(b) are also increasing with increasing Pr content $x$ with a plateau-like behavior for intermediate compositions $x \approx 0.2$ and $x \approx 0.8$. This implies that Pr substituting for Y and/or Ba acts as a source of crystal defects, the Pr123 phase being a strained phase compared to Y123.

### *3.2. Micro-Raman analysis*

Typical Raman spectra for the two scattering polarizations, $xx$ and $zz$ (incident and scattered light polarization parallel or perpendicular to the $CuO_2$ planes, respectively), are presented in figures 8(a) and (b), respectively, for selected Pr concentrations.

In the $xx$ scattering polarization spectra of (Y–Pr)123, the low energy modes at ≈115 $cm^{-1}$ and ≈150 $cm^{-1}$ for $x = 0.0$ are due to the Ba and Cu2 atoms, respectively. With increasing amount of Pr substitution the spectral shape of the Ba phonon becomes extremely asymmetric (Fano shape). Especially in the pure Pr123 compound this mode has an unusual shape, not observed before in the full region of oxygen doping [44]. If this extremely asymmetric shape in the low energy side of the spectrum could be attributed to the coupling with the carriers, it would imply a further increase of the hole carriers with Pr doping. This can also be due to the partial Pr substitution for Ba, which will shift the phonon and create the extremely asymmetric Fano shape of the Ba/Pr mixed mode. The intensity of the Cu2 atoms slightly increases with the amount of Pr. This points to a decrease of the amount of carriers within the $CuO_2$ planes, which modifies the screening of the Cu2 phonon [44]. In the other polarization, the two low energy phonons have the same characteristics independent of the amount of Pr (figure 8(b)). But the energy of the Ba mode is continuously shifting to higher values with the amount of Pr [12]. Besides, the width of this mode increases

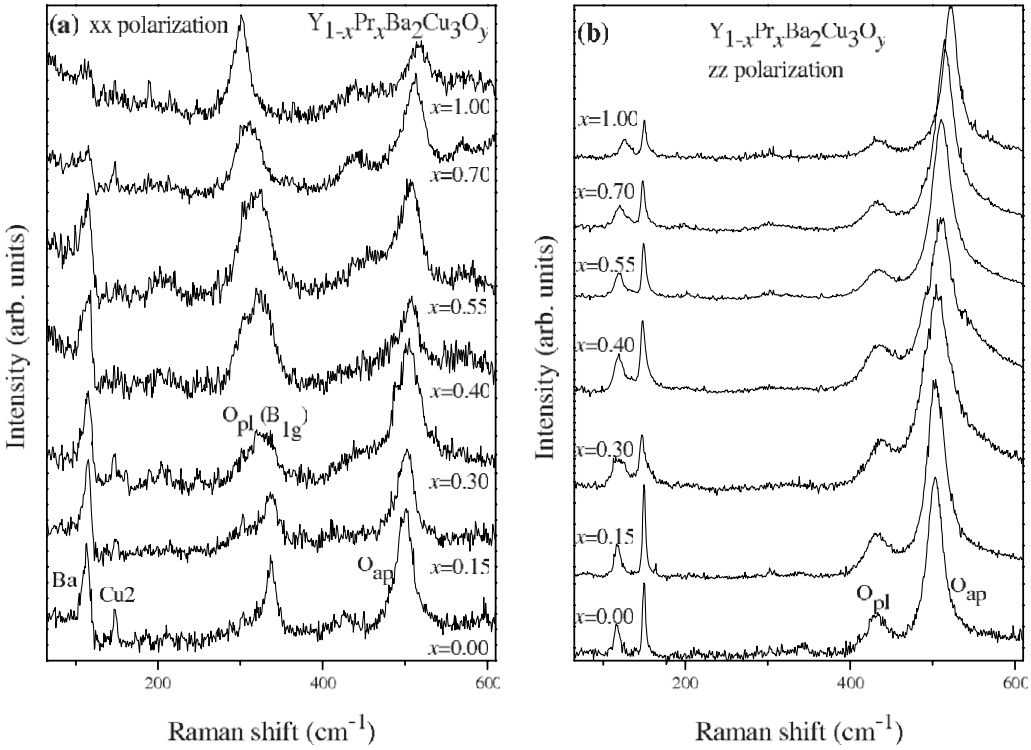


**Figure 8.** Typical micro-Raman spectra in the $xx$ (a) and $zz$ (b) scattering polarizations for selected (Y–Pr)123 concentrations.

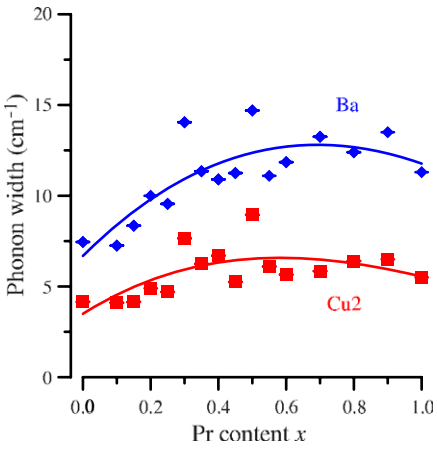


**Figure 9.** Variation of the Ba and Cu2 phonon width with the Pr content $x$ in the (Y–Pr)123 compounds.

continuously with the Pr substitution (figure 9). These two effects explain the abnormal behavior of the phonon observed in the $xx$ polarization. The same energy shift is induced from the $xx$ spectra, although it is more difficult to extract accurate values of the peak position from an asymmetric Fano shape fit.

In all Y123 rare-earth substitutions, the $B_{1g}$-like mode (out-of-phase motion of plane oxygen atoms, observed in the $xx$ scattering geometry) shows the most impressive modifications. In the pure Y123 this phonon has the normal asymmetric Fano shape apparently related with its coupling to the carriers within the $CuO_2$ planes. With increasing Pr substitution its energy shifts from ≈340 $cm^{-1}$ in Y123 to ≈302 $cm^{-1}$ in Pr123 (figure 8(a)). Besides, it is clear that this band is composite for intermediate Pr concentrations and it becomes much wider with a modified lineshape. As has been done in the past with other rare-earth substitutions for Y in Y123 [9, 10], this behavior can be interpreted as evidence for the development of three phases, one Y123, one Pr123 and a mixed YPr123 phase of almost the nominal amount of Pr. For 100% Pr substitution only the mode at ≈302 $cm^{-1}$ remains, which apparently is the $B_{1g}$-like phonon of the pure Pr123 compound. This phonon is more symmetric than in the pure Y123 (figure 8(a)), an indication for the suppression of carriers within the $CuO_2$ planes. This is in agreement with the results obtained by the BVS calculations based on the XRD bond distance data.

In the intermediate Pr content, we can deconvolute this phonon into three peaks that correspond to the above-mentioned phases and reveal the energy of the mode of the anticipated intermediate phase. Based on the dependence of the $B_{1g}$ phonon energy on the rare-earth ionic radius [45], one can associate the energy of the intermediate phase mode with an average ionic radius and from that estimate the chemical composition of this mixed phase. From this analysis, we conclude that the mixed phase approximately corresponds to the nominal Pr composition. Furthermore, one can calculate the relative contribution of the three peaks to the total $B_{1g}$ band and from that get an estimate of the percentage volume fraction for each of the three phases. This is presented in table 4, where characteristic changes at the critical compositions 0.2 (appearance of the intermediate and the Pr123 phases), 0.6 (disappearance of the Y123 pure phase) and 0.8 (considerable increase of the pure Pr123 and strong reduction of the intermediate phase) can be seen. In table 4 are also shown

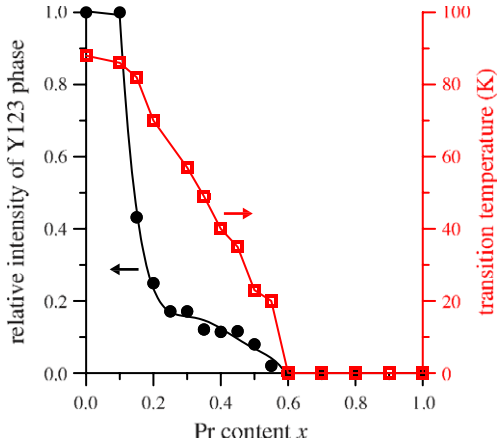


**Figure 10.** (Left) The relative amount of the Y123 phase as induced from the deconvolution of the $B_{1g}$-symmetry Raman-active band. (Right) The transition temperature $T_c$ of the $Y_{1-x}Pr_xBa_2Cu_3O_y$ compounds as a function of Pr doping $x$. The solid line is a guide for the eye.

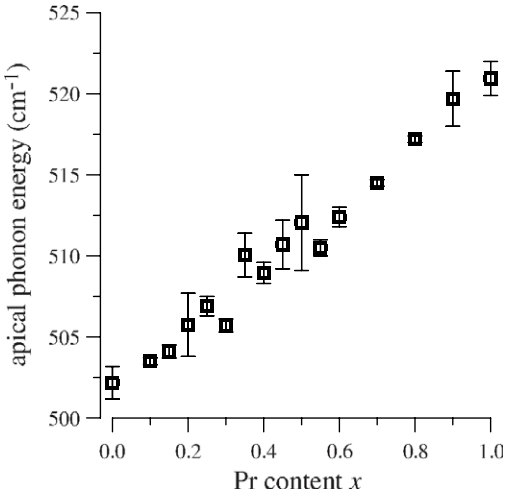


**Figure 11.** Dependence of the apical oxygen phonon energy of the (Y–Pr)123 compounds on the Pr content $x$.

**Table 4.** Relative amounts of the three phases Y123, Y–Pr123 and Pr123 as induced by the deconvolution of the $B_{1g}$-symmetry Raman-active band. Also shown the $T_c$ and $\Delta T_c$. The compounds with $x \geqslant 0.60$ did not show a superconducting transition to the lowest temperature measured (4 K). The $T_c$ of the compound $x = 0.25$ was not measured.

| $x$ | Y123 phase | Y–Pr123 phase | Pr123 phase | $T_c$ | $\Delta T_c$ |
|---|---|---|---|---|---|
| 0.00 | 1.00 | 0.00 | 0.00 | 88 | 22 |
| 0.10 | 1.00 | 0.00 | 0.00 | 86 | 29 |
| 0.15 | 0.43 | 0.57 | 0.00 | 82 | 23 |
| 0.20 | 0.25 | 0.75 | 0.00 | 70 | 23 |
| 0.25 | 0.17 | 0.68 | 0.15 | | |
| 0.30 | 0.17 | 0.69 | 0.14 | 57 | 29 |
| 0.35 | 0.12 | 0.53 | 0.35 | 49 | 28 |
| 0.40 | 0.11 | 0.70 | 0.19 | 40 | 24 |
| 0.45 | 0.12 | 0.66 | 0.22 | 35 | 29 |
| 0.50 | 0.08 | 0.64 | 0.28 | 23 | 9 |
| 0.55 | 0.02 | 0.77 | 0.21 | 20 | 11 |
| 0.60 | 0.00 | 0.70 | 0.30 | — | — |
| 0.70 | 0.00 | 0.70 | 0.30 | — | — |
| 0.80 | 0.00 | 0.59 | 0.41 | — | — |
| 0.90 | 0.00 | 0.00 | 1.00 | — | — |
| 1.00 | 0.00 | 0.00 | 1.00 | — | — |

the superconducting transition temperature $T_c$ values and the corresponding diamagnetic transition width $\Delta T_c$ (10%–90%) of all samples. The transition temperature $T_c$ is suppressed very drastically when Pr substitutes for Y, reaching a value close to zero at a critical composition $x_c = 0.6$ (figure 10), in agreement with previous observations [1].

In the high energy part of the $zz$ polarization spectra (figure 8(b)) the phonon at ≈430 cm$^{-1}$ for $x = 0.00$ corresponding to the in-phase motion of the plane oxygen atoms remains almost constant in energy. The energy of this phonon is very sensitive to the amount of oxygen and corresponds to samples with optimum to overdoped oxygen concentration [11], in complete agreement with the measurement of the oxygen content in the samples. Variations in its linewidth reflect variations in the oxygen content and the coexistence of the optimum and overoxygenated phases.

The phonon at ≈503 cm$^{-1}$ (for $x = 0.0$) corresponds to the apical oxygen and shifts almost linearly to higher energies with increasing amount of Pr (figure 11), mainly as a result of the decreasing bond distance Cu2–O1. A similar behavior has been observed in pure Y123, where with the increasing amount of oxygen doping the Cu2–O1 distance decreases accompanied by an increase in the apical phonon energy [44]. The dependence of the apex phonon energy on the Cu2–O1 bond distance (figure 12) follows the general trend found by the oxygen doping [44], but it also shows some anomaly around the $0.2 < x < 0.8$ region. This anomaly can be explained by the phase separation found from the $B_{1g}$ mode for the same Pr doping level. The linewidth of the apex mode increases for intermediate Pr concentrations (figure 13) as a result of the formation of phases with different amounts of Pr content, in agreement with the results obtained from the spectral modifications in the $B_{1g}$ phonon (figure 8(a)). In any case, the pronounced effects observed in the $B_{1g}$-like phonon are not repeated here. This is partially due to the much weaker dependence of the apex phonon energy on the Pr substitution (5% change from Y123 to Pr123 compared with 10% of the $B_{1g}$ mode). Besides, the strong dependence of the apex $A_g$-symmetry phonon mode on the amount of oxygen content or the ordering of the chain oxygen atoms complicates the analysis. The larger width of the Pr123 compared with the pure Y123 (figure 13) could reflect changes induced along the $ab$ plane from the random ordering of the chains, in agreement with the presence of stacking faults evidenced from the XRD profiles.

## 4. Discussion

The evolution of the orthorhombic lattice parameters with Pr content (figure 2) is indicative of an anisotropic chemical stress induced by the substitution of Pr for Y. The $c$ axis exhibits a smaller expansion upon Pr substitution with respect to the $a$ and $b$ axes. It has been argued that the so-called $c$ lattice anomaly is a pure size effect due to the substitution of the

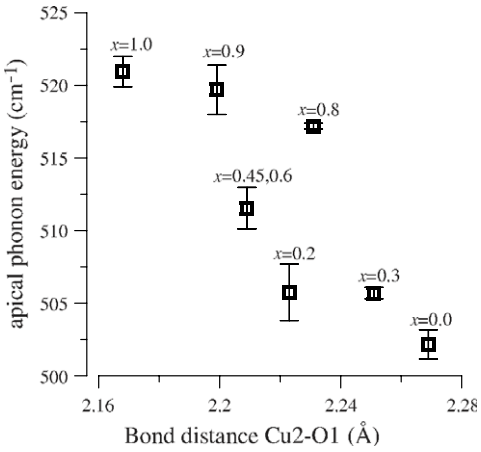


**Figure 12.** Dependence of the apical oxygen phonon energy on the Cu2–O1 bond distance.

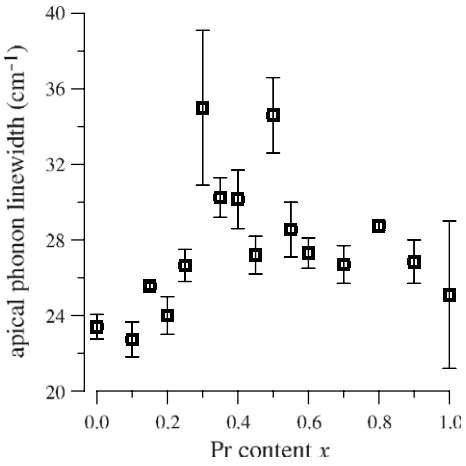


**Figure 13.** Variation of the apical oxygen phonon linewidth with the Pr content $x$ in the (Y–Pr)123 compounds.

smaller Pr ion for the bigger Ba ion [2]. Inspection of the changes of interatomic Cu2–Cu2 and Cu1–Cu2 distances along the $c$ axis (figure 3(a)), in comparison with those observed in the (Y–La)123 solid solution, suggests that the effect might be much more complicated. Although one of the origins of the anomalously short $c$ axis may be the substitution of Pr for Ba, charge effects across the $CuO_2$ planes may also play a crucial role besides the size in the Pr123 structure. The substitution of the bigger Pr for the smaller Y in the solid solution $Y_{1-x}Pr_xBa_2Cu_3O_y$ results generally in increasing tensile internal strains on the Pr–$O_{pl}$ and Cu2–$O_{pl}$ bonds with increasing Pr content $x$. However, both the Cu2–Cu2 and the Pr–$O_{pl}$ bonds in the Pr123 compound have been found to be smaller than expected from the trend of the rare-earth ionic sizes.

No remarkable change is observed at the critical composition $x_c = 0.6$ in all bond lengths obtained from the average structure. On the other hand, subtle modifications observed on the Cu2–O3 (figure 3(b)) and the Pr–O3 (figure 3(c)) bonds, on the Cu2–O3–Cu2 angle (figure 3(e)) and on the internal strain at the Y/Pr site (figure 5) at compositions $x \approx 0.2$ and $x \approx 0.8$ appear to correlate with the modifications of the $B_{1g}$ mode of the Raman spectra and the formation of the phases shown in table 4. The microstructural features observed with XRD provide additional evidence for the formation of these seemingly nanoscopic phases. The diffraction line profile analysis revealed the presence of enhanced microstrains in the pure Pr123 phase. The variation of microstrains with the Pr content $x$ correlates with the amount of the Pr123 phase that develops upon Pr substitution (figure 6). The pure Pr123 phase, appearing at $x \approx 0.2$, increases considerably for $x \geqslant 0.8$ accompanied by microstrains. At intermediate compositions $0.2 < x \leqslant 0.8$ the latter seem to be almost constant following a plateau-like behavior of the development of the Pr123 phase. This plateau is most probably associated with the development of the intermediate phase. At the same intermediate compositional range $0.2 < x \leqslant 0.8$, the average size of the coherently diffracting domains has been found to decrease down to a minimum value of approximately 300 nm at $x \approx 0.5$. The size of the domains as proposed by Raman data for the intermediate compositions could be much smaller than the domains obtained by XRD. However, the latter have been obtained assuming isotropic domains, which may not be the case. The real sizes can be lower but we are mostly interested in extracting the evolution of the size rather than the precise values. The decrease of diffracting domains at intermediate compositions and the apparent correlation of microstrain variation with the amount of the pure Pr123 phase clearly supports the phase separation scheme anticipated by Raman data.

The synchrotron powder XRD and micro-Raman results presented so far agree on the formation of different nanoscopic environments in the Y–Pr123 solid solution upon Pr substitution. From the Raman data it appears that there are three such phases: one pure Y123, one pure Pr123 together with an intermediate one having approximately the nominal composition $Y_{1-x}Pr_xBa_2Cu_3O_y$. The reduction in $T_c$ seems to correlate with the reduction of the Y123 superconducting phase (figure 10 and table 4, where the percentage volume fraction of the Y123 phase becomes zero for $x = 0.60$, exactly where $T_c = 0$). Assuming that the pure Pr123 phase is non-superconducting the suppression of superconductivity in the solid solution $Y_{1-x}Pr_xBa_2Cu_3O_y$ could be understood by taking into account the evolution of the three phases upon Pr content $x$.

The formation of the pure P123 phase upon Pr substitution correlates with characteristic features obtained from the XRD analysis such as the increase of: (1) local lattice disorder at the Cu and Ba atoms, (2) anisotropic microstrain due to crystal defects and (3) the increase of the amount of $Pr_{Ba}$ antisite defects. It also agrees with the micro-Raman results of increasing energy and distorted profile of the Ba phonon mode. These suggest that enhanced lattice disorder and distortion in the Ba ion environment is present in the pure P123 phase. Two questions usually arise; whether the presence of $Pr_{Ba}$ antisite defects unambiguously take place in the Pr123 structure and how crucial parameter is such Pr substitution at the Ba site for the suppression of superconductivity. Both questions have been under dispute for a long time [1]. On the one hand, the

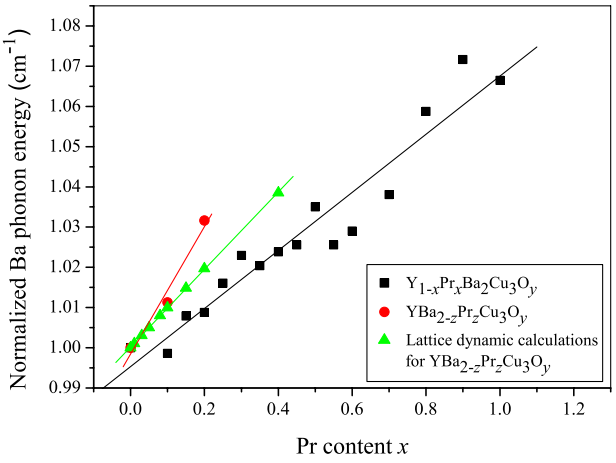


**Figure 14.** The normalized Ba phonon energy in connection with the Pr content $x$ in $Y_{1-x}Pr_xBa_2Cu_3O_y$ (squares) and $YBa_{2-z}Pr_zCu_3O_y$ (circles). Triangles indicate data obtained from lattice dynamic calculations for $YBa_{2-z}Pr_zCu_3O_y$.

presence of Pr at the Ba site cannot be accurately determined by XRD and neutron diffraction experiments due to the similar scattering factors of Pr and Ba. Concerning the other question, different mechanisms have been proposed in order to interpret the suppression of superconductivity in Pr123 based on the Pr substituting for Ba, without general agreement with the many opposing experimental data (see [1] and discussion herein).

In order to investigate the first question, we compare the Raman results obtained from two sets of compounds $Y_{1-x}Pr_xBa_2Cu_3O_y$ ($0 \leqslant x \leqslant 1$) ($zz$ spectra, figure 8(b)) and $YBa_{2-z}Pr_zCu_3O_y$ for the Ba phonon with lattice dynamic calculations based on GULP (figure 14) [46]. In both compounds the measured phonon energy increases with increasing Pr content [12], at first glance violating the harmonic mass law (the heavier Pr partially migrating to the Ba site would yield lower values for the phonon energy). A similar increase in the Ba phonon energy has been reported in the $YBa_{2-x}La_xCu_3O_y$ where the trivalent La substitutes for the divalent Ba [47]. This suggests a possible Ba phonon energy dependence on the site charge. Our lattice dynamic calculations indicate that this is really the case. Assuming an increased valence at the Ba site by the apparent Pr substitution the energy of the Ba $A_g$-symmetry phonon increases, in good agreement with the experimentally measured values (figure 14).

Knowing from previous work that the Ba phonon energy does not depend on the rare-earth substitution at the Y site [8, 10], we have considered the observed modification as a result of the Pr substitution for Ba [12]. By comparing the variation of the Ba phonon energy vs the Pr content for the $Y_{1-x}Pr_xBa_2Cu_3O_y$ and $YBa_{2-z}Pr_zCu_3O_y$ compounds we could obtain an estimate of the amount of nominal Pr substituting for Ba in the $Y_{1-x}Pr_xBa_2Cu_3O_y$ that induces the same phonon shift as the antisite defects $Pr_{Ba}$ in the Y–Pr123 nominal compound [12]. The values obtained by Raman are higher than those obtained by the Rietveld refinement but this disagreement could be understood taking into account the limitations of the XRD analysis in this case mentioned above. Besides, the nominal Pr substitution for Ba may differ from the real one, since some part of Pr will occupy the Y site. For $x \approx 0.6$, where the superconductivity disappears in (Y–Pr)123, the amount of Pr substituting for Ba is ≈11% [12], in agreement with Blackstead *et al* [2].

Although ≈40% of Pr at the Ba sites in $PrBa_{1.6}Pr_{0.4}Cu_3O_y$ phase was found to provoke a structural symmetry transition and excess of oxygen [48], no such effects were observed in our measurements (oxygen content, Raman and XRD). On the contrary, XRD patterns have shown increased amounts of planar defects such as stacking faults in the pure Pr1237. These stacking faults, being most probably the insertion of an extra Cu–O chain between adjacent Ba–O layers, reduce the average valence of Cu atoms in the structure, compensating the valence change introduced at the $Ba^{2+}$ site by its partial substitution by the $Pr^{+3}$ ion. The increased amount of stacking faults in the Pr123 phase relative to that of the Y123 phase is thus an indirect additional manifestation of the $Pr^{+3}$ substitution for $Ba^{2+}$. In this way, the number of carriers around the Ba site will increase with the Pr substitution for Ba, justifying the increased asymmetry of the Ba $A_g$ phonon in the Raman spectra (figure 8(a)).

Our Raman data in connection with the XRD analysis proves unambiguously that extended partial substitution of Pr for Ba takes place in the Pr123 structure. It is worth mentioning that our previous Raman investigations on Y–La123 compounds, prepared carefully under the same conditions as the Y–Pr123, have not shown appreciable changes in both Ba phonon energy and shape, implying a very limited, if any, $La^{3+}$ substitution for $Ba^{2+}$ [10]. These samples exhibit only a limited reduction of the transition temperature [10]. On the contrary, Guillaume *et al* [27] have reported that an occupation of 15% $La^{3+}$ ions at the $Ba^{2+}$ site in their La123 sample, measured with neutron diffraction, reduces $T_c$ to zero. Such La substitution for Ba will induce a shift in the Ba phonon energy [47], which had not been observed in our data [10]. This is an indication that the possibility of creating antisite $La_{Ba}$ defects may depend on the preparation conditions.

We discuss next the suppression of superconductivity in the Pr123 compound. Ca substitution for Y induces an overdoping in Y1237, also reducing the transition temperature [11]. It appears that the two cases (partial $Ca^{2+}$ substitution for $Y^{3+}$ or partial $Pr^{3+}/La^{3+}$ substitution for $Ba^{2+}$) have a common origin; the modification of the charges across the $CuO_2$ planes ($Y^{+3}$ and $Ba^{+2}$ ions). By 20% Ca substitution for Y the Y–Ca1237 compound loses its superconductivity property [11]. In the present case, we have calculated that roughly 11% substitution of Pr for Ba, i.e. a roughly equivalent amount of electric field reduction across the $CuO_2$ planes, again induces the loss of superconductivity. The charge distribution across the $CuO_2$ planes first of all will affect the amount of carriers in the planes. The $Pr^{3+}$ for $Ba^{2+}$ substitution will reduce the amount of carriers, though the effect may not be so pronounced due to the stacking faults and the apparent addition of an extra CuO plane. In addition, the modified charge across the $CuO_2$ planes must couple with the $\pi$ orbitals of $O_{pl}$, rearranging the carriers within the planes.

Several mechanisms have been proposed that can provide an explanation for the real effect of the Pr doping [49]. It seems that the main effects are related to the partial Pr substitution for Ba resulting in the modification of the ion charges across the $CuO_2$ superconducting planes.

Concerning the driving mechanism of phase separation in the solid solutions Y-R123, in the La substitution for Y we have found that it seems to be mainly the volume effect [10]. In the case of the Y–Pr123 there are additional parameters that play a role, such as the charge distribution and the partial occupation of the Ba site, besides the volume effect. In both cases, it appears that the phase separation must be taken under consideration in order to understand the $T_c$ dependence on doping.

## 5. Conclusions

Concluding, we have shown with high resolution x-ray powder diffraction and micro-Raman measurements on optimally doped or overdoped polycrystalline $Y_{1-x}Pr_xBa_2Cu_3O_y$ ($0 \leqslant x \leqslant 1$) samples that Pr substituting for Y and/or Ba acts as a source of crystal defects, the Pr123 phase being a strained phase compared to the Y123. Extended partial substitution of Ba by Pr takes place in the Pr123 structure and the Pr substitution at the Ba site is a crucial parameter suppressing $T_c$, through the increased charge of the Pr ion at the 'wrong' site. A mechanism in yttrium cuprates is related to the excess charge across the $CuO_2$ planes, which seems to play some role in the suppression of superconductivity. Moreover the coexistence of locally different rare-earth nanoscopic environments (phases Y123, Pr123 and a mixed YPr123 phase) can give a clue to the way that $T_c$ decreases with composition.

## Acknowledgments

We thank ESRF for the provision of synchrotron beam time and Dr Wouter van Beek for useful discussions and assistance during data collection at BM01B. Work partially supported by the Special Research Account (Kapodistrias) of University of Athens and CoMePhS (STRP project of EU).

## References

[1] Akhavan M 2002 *Physica* B **321** 265 and references therein
[2] Blackstead H A, Dow J D, Felner I and Yelon W B 2001 *Phys. Rev.* B **63** 094517
Blackstead H A and Dow J D 2000 *Solid State Commun.* **115** 137
[3] Mohammadizadeh M R and Akhavan M 2003 *Phys. Rev.* B **68** 104516
[4] Harada T and Yoshida K 2002 *Physica* C **383** 48
[5] Yoshida K 2000 *Physica* B **284–288** 644
[6] Yoshida K 1999 *Phys. Rev.* B **60** 9325
[7] Muroi M and Street R 1998 *Physica* C **301** 277
[8] Calamiotou M, Gantis A, Palles D, Lampakis D, Liarokapis E and Koufoudakis A 1998 *Phys. Rev.* B **58** 15238
[9] Bogachev G, Abrashev M, Iliev M, Poulakis N, Liarokapis E, Mitros C, Koufoudakis A and Psyharis V 1994 *Phys. Rev.* B **49** 12151
[10] Gantis A, Calamiotou M, Palles D, Lampakis D and Liarokapis E 2003 *Phys. Rev.* B **68** 064502
[11] Liarokapis E, Palles D, Lampakis D, Bottger G, Conder K and Kaldis E 2005 *Phys. Rev.* B **71** 014303
[12] Palles D, Lampakis D, Siranidi E, Liarokapis E, Gantis A and Calamiotou M 2007 *Physica* C **460–462** 922
[13] Kaldis E 2001 Oxygen nonstoichiometry and lattice effects in $YBa_2Cu_3O_y$ *Handbook of Physics and Chemistry of the Rare Earths* vol 31 *High Temperature Superconductors* ed L Eyring *et al* (Amsterdam: North-Holland Elsevier)
[14] Gasumyants V E, Elizarova M V and Suryanarayanan R 2000 *Phys. Rev.* B **61** 12404
[15] Gasumyants V E, Vladimirskaya E V and Patrina I B 1997 *Phys. Solid State* **39** 1352
[16] Cao G, Qian Y, Chen Z and Zhang Y 1995 *J. Phys. Chem. Solids* **56** 981
[17] Karpinski J, Conder K and Kaldis E 1988 *Physica* C **153–155** 401
[18] Gualtieri A F, Ferrari S, Galli E, Di Renzo F and van Beek W 2006 *Chem. Mater.* **18** 76
[19] Fitch A N 2004 *J. Res. Natl Inst. Stand. Technol.* **109** 133
[20] Larson A C and von Dreele R B 2004 General structure analysis system (GSAS) *Los Alamos National Laboratory Report LAUR* pp 86–748
[21] Jorgensen J D, Veal B W, Paulikas A P, Nowicki L J, Crabtree G W, Claus H and Kwok W K 1990 *Phys. Rev.* B **41** 1863
[22] Guskos N, Likodimos V, Londos C A, Psyharis V, Mitros C, Koufoudakis A, Gamari-Seale H, Windsh W and Metz H 1995 *J. Solid State Chem.* **119** 50
[23] Thomson P T, Cox D E and Hastings J B 1987 *J. Appl. Crystallogr.* **20** 79
[24] Stephens P 1999 *J. Appl. Crystallogr.* **32** 281
[25] Sharma R P, Rotella F J, Jorgensen J D and Rehn L E 1991 *Physica* C **174** 409
[26] Alfred-Duplan C, Vacquier G, Marfaing J, Ritter H and Ihringer J 2000 *Ann. Chim. Sci. Mater.* **25** 281
[27] Guillaume M, Allenspach P, Mesot J, Roessli B, Staub U, Fischer P and Furrer A 1993 *Z. Phys.* B **90** 13
[28] Altermatt D and Brown I D 1985 *Acta Crystallogr.* B **41** 240
Brown I D and Altermatt D 1985 *Acta Crystallogr.* B **41** 244
[29] Brown I D 1991 *J. Solid State Chem.* **90** 155
[30] Rao G H, Bärner K and Brown I D 1998 *J. Phys.: Condens. Matter* **10** L757
[31] Karpinski J, Kazakov S M, Angst M, Mironov A, Mali M and Roos J 2001 *Phys. Rev.* B **64** 094518
[32] Tallon J L 1990 *Physica* C **168** 85
[33] Tallon J L, Benseman T, Williams G V M and Loram J W 2004 *Physica* C **415** 9
[34] Willliamson G K and Hall W H 1953 *Acta Metall.* **1** 22
[35] Balzar D 1993 *J. Res. Natl Inst. Stand. Technol.* **98** 321
[36] Kramer M J, Chumbley L S, McCallum R W, Nellis W J, Weir S and Kvam E P 1990 *Physica* C **166** 115
[37] Li D J, Shibahara H, Zhang J P, Marks L D, Marcy H O and Song S 1988 *Physica* C **156** 201
[38] Van Tendeloo G, Krekels T and Amelinckx S 1991 *Phil. Mag. Lett.* **63** 189
[39] Xia J A, Munroe P R, Wang R K, Ren H T, Zhao Y and Dou S X 1995 *Physica* C **241** 142
[40] Balogh L, Ribárik G and Ungár T 2006 *J. Appl. Phys.* **100** 023512
[41] Casas-Cabanas M, Palacin M R and Rodriguez-Carvajal J 2005 *Powder Diffr.* **20** 334
[42] David W I F, Moze O, Licci F, Bolzoni F, Cywinski R and Kilcoyne S 1989 *Physica* B **156–157** 884
[43] Rand M, Langford J I and Abell J S 1993 *Phil. Mag.* B **68** 17
[44] Palles D, Poulakis N, Liarokapis E, Conder K, Kaldis E and Müller K A 1996 *Phys. Rev.* B **54** 6721

[45] Rosen H J, Macfarlane R M, Engler E M, Lee V Y and Jacowitz R D 1988 *Phys. Rev.* B **38** 2460
[46] Gale J D 1997 GULP—a computer program for the symmetry adapted simulation of solids *JCS Faraday Trans.* **93** 629
Gale J D 1996 *Phil. Mag.* B **73** 3
Gale J D and Rohl A L 2003 *Mol. Simul.* **29** 291
[47] Wegerer R, Thomsen C, Cardona M, Bornemann H J and Morris D E 1996 *Phys. Rev.* B **53** 3561
[48] Luo H M *et al* 2000 *Phys. Rev.* B **61** 14825
[49] Fehrenbacher R and Rice T M 1993 *Phys. Rev. Lett.* **70** 3471